Investigating the Ultracompact X-Ray Binary Candidate SLX 1735-269 with NICER and NuSTAR

D. L. Moutard[1] , R. M. Ludlam[1] , M. Sudha[1] , D. J. K. Buisson[2], E. M. Cackett[1] , N. Degenaar[3] , A. C. Fabian[4] ,
P. Gandhi[5] , J. A. García[6] , A. W. Shaw[7] , and J. A. Tomsick[8]

[1] Department of Physics & Astronomy, Wayne State University, 666 West Hancock Street, Detroit, MI 48201, USA; david.moutard@wayne.edu
[2] Independent Researcher, UK
[3] Anton Pannekoek Institute for Astronomy, University of Amsterdam, Science Park 904, 1098 XH Amsterdam, Netherlands
[4] Institute of Astronomy, University of Cambridge, Madingley Road, Cambridge CB3 0HA, UK
[5] School of Physics and Astronomy, University of Southampton, University Road, Southampton SO17 1BJ, UK
[6] Cahill Center for Astronomy and Astrophysics, California Institute of Technology, 1200 E. California Boulevard, MC 290-17, Pasadena, CA 91125, USA
[7] Department of Physics and Astronomy, Butler University, Indianapolis, IN 46208, USA
[8] Space Sciences Lab, University of California, Berkeley, 7 Gauss Way, Berkeley, CA 94720, USA

Abstract

We present two simultaneous NICER and NuSTAR observations of the ultracompact X-ray binary (UCXB) candidate SLX 1735−269 while the source was in two different spectral states. Using various reflection modeling techniques, we find that XILLVERCO, a model used for fitting X-ray spectra of UCXBs with high carbon and oxygen abundances is an improvement over RELXILL or RELXILLNS, which instead contains solar-like chemical abundances. This provides indirect evidence in support of the source being ultracompact. We also use this reflection model to get a preliminary measurement of the inclination of the system, $i = 57^{+23}_{-7}$ degrees. This is consistent with our timing analysis, where a lack of eclipses indicates an inclination of $i < 80°$. The timing analysis is otherwise inconclusive, and we cannot confidently measure the orbital period of the system.

Unified Astronomy Thesaurus concepts: Low-mass x-ray binary stars (939); X-ray binary stars (1811); Neutron stars (1108)

1. Introduction

A low-mass X-ray binary (LMXB) is a system comprised of a compact object, a neutron star (NS) or black hole, interacting gravitationally with a main-sequence, subgiant, or red giant star (which we may call canonical LMXBs). In these systems, the companion star fills its Roche lobe, and then deposits matter into an accretion disk surrounding the compact object. An ultracompact X-ray binary (UCXB) is a subclass of LMXB differentiated by a much shorter orbital period, generally defined to be <80 minutes, compared to the typical periods of hours to days that are seen in LMXBs (Bahramian & Degenaar 2023). This shorter period is caused by a more compact companion than a main-sequence star, such as a white dwarf (WD) or helium star (Nelson et al. 1986; Savonije et al. 1986). These companions have a notably different chemical composition than their main-sequence or red giant counterparts, often lacking hydrogen and helium, and containing an over-abundance of carbon and oxygen. LMXBs are well-studied systems, used to understand generally accretion physics and the physics of compact objects and in the era of multimessenger astronomy they can be considered as a source of gravitational waves (Chen et al. 2020).

In LMXB and UCXB systems it is believed that the X-rays originate from the region of closest accretion inflow, where material transitions from the accretion disk to falling onto the compact object. Near the compact object we expect an X-ray corona—a source of nonthermal photons generated from the

Compton up-scattering of seed photons from the accretion disk, or in the case of an NS LMXB, perhaps a boundary layer of material that surrounds the surface of the NS (Syunyaev et al. 1991). Some of these hard X-rays should reach the observer directly, but we also expect to observe the interaction between these photons and the rest of the LMXB system. This can manifest as reflection features, where coronal X-rays scatter off the disk, and are then reprocessed. A common feature of this reflection is the Fe Kα line around 6.4 keV, but the unique composition of UCXBs means that we may also see an O VIII Lyα feature at around 0.67 keV. In UCXBs we also sometimes see a suppression of the Fe Kα line (Koliopanos et al. 2014). These reflected features experience a relativistic broadening, as the disk material orbits rapidly around the compact object. In X-ray studies, these features are believed to arise from the region of the disk nearest the compact object (Fabian et al. 1989). Because of this, we can use the broadening of the reflected emission to determine the radius at which the innermost region of the disk sits. For NS LMXBs, this can provide an upper bound on the radius of the NS, which is important for understanding the NS equation of state (Cackett et al. 2008; Miller et al. 2013; Ludlam et al. 2017). For a recent comprehensive review of reflection studies in NS LMXBs, see Ludlam (2024). In reflection studies we are therefore able to model the spectral contribution from 3–4 different components: nonthermal photons from the corona, thermal photons from the disk, reflected emission, and/or thermal emission from the NS and boundary layer itself.

SLX 1735−269 was discovered in 1985 during the Spacelab 2 mission during X-ray observations of the Galactic center (Skinner et al. 1987). The existence of thermonuclear X-ray bursts (Bazzano et al. 1997) as well as the spectral shape

Table 1
SLX 1735−269 Observation Information

Obs.	Mission	Sequence ID	Obs. Start (UTC)	Exp. (ks)
1	NuSTAR	30601007002	2020-04-15 16:36:09	31.0
	NICER	3604020101	2020-04-15 19:59:00	1.7
2	NuSTAR	30601007004	2021-04-18 06:01:09	31.4
	NICER	3604020104	2021-04-18 06:13:52	4.8

(David et al. 1997) demonstrates that the compact object in this system is an NS, but the companion is still poorly understood. in't Zand et al. (2007) proposes the UCXB candidacy based on its low luminosities and the frequency of bursts. It has been found that almost all UCXBs occupy the lowest accretion rate regimes, and accretion rate is directly proportional to the luminosity. An increased burst recurrence time can also be explained by a lower accretion rate. Molkov et al. (2005) detects long bursts in this system as well, up to ∼2 ks. This is explained to likely be the burning of a mixed pile of hydrogen and helium. This helium burning scenario has been used to explain long bursts in UCXBs in the past (Cumming et al. 2006). However, lack of optical spectra to confirm the presence of carbon or oxygen lines and no studies of the orbital period means we cannot verify the UCXB nature of SLX 1735−269. The source is localized with subarcsecond accuracy in Chandra at Galactic coordinates $\ell = 0.796$, $b = 2.400$ (Wilson et al. 2003). A possible optical counterpart that is spatially coincident with the X-ray source exists near the edge of the Chandra positional uncertainty for SLX 1735−269, though it has not been spectrally identified. The counterpart also exhibits a shape which cannot be ruled out as having a double nature, so estimates in position and magnitude have additional uncertainty (Zolotukhin & Revnivtsev 2011). Because SLX 1735−269 is so close to the Galactic center, the high column density of neutral hydrogen may make optical studies to search for key UCXB features difficult. In this paper we use simultaneous NICER and NuSTAR observations with reflection modeling techniques to better understand the source. In Section 2 we discuss the details of the data reduction and observations and in Section 3 we show the results of our spectral analysis. In Section 4 we discuss the implications of these results, then summarize the results and conclude the paper.

2. Observations and Data Reduction

SLX 1735−269 was observed on two separate occasions roughly 1 yr apart with both NICER and NuSTAR simultaneously. More detailed information about these observations can be seen in Table 1. We reduce the NuSTAR data using NUSTARDAS v2.1.2 and CALDB 20230816. The light curves and spectra were extracted using regions with a diameter of 100″ centered on the source. The backgrounds were also extracted using 100″ apertures, but centered elsewhere. Obs 2 displayed some contamination from stray light, but these do not overlap the source itself, and backgrounds were selected such that they did not contain this stray light contamination. The NICER data were calibrated using NICERDAS 2023-08-22_v011a and CALDB 20221001. This calibration was done first by the use of NICERL2 for geomagnetic prefiltering. The NIMAKETIME command was used to generate good time intervals (GTIs) with low particle background (planetary K-index, KP < 5). Other cuts are made to eliminate particle
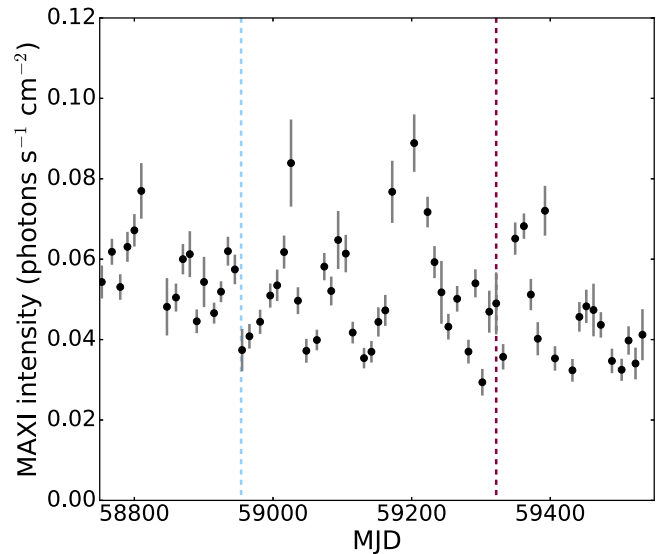

Figure 1. A long-term MAXI light curve for the source. Vertical lines indicate the dates at which Obs 1 (left, blue) and Obs 2 (right, red) occur. We see that Obs 1 occurs during a lower flux state than Obs 2. The MAXI data are binned to 10 days.
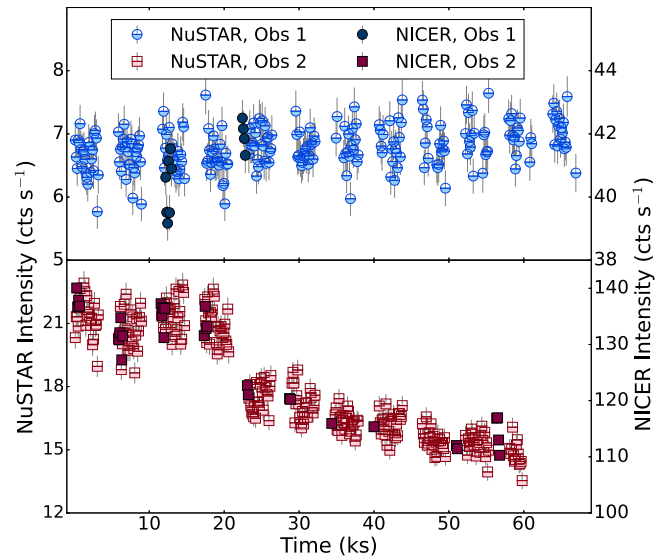

Figure 2. Light curve for the NuSTAR (half-filled) and NICER (filled) observations of SLX 1735−269 binned to 128 s. The top panel represents Obs 1 (blue circles) and the bottom represents Obs 2 (red squares). Only one NuSTAR focal plane module (FPM) is shown for clarity.

overshoots (COR_RANGE 1.5–20 and OVERONLY_RANGE 0–2). Then NICERL3-SPECT is used to create NICER spectra, background, and response files and NICERL3-LC is used to generate light curves. These instances of NICERL3-SPECT and NICERL3-LC utilize the 3C50 background model (Remillard et al. 2022). Figure 1 shows the time of these observations on a MAXI light curve.

Neither observation contained a Type I X-ray burst, so no additional filtering was done. Both the NICER and NuSTAR data are rebinned using the optimal binning method (Kaastra & Bleeker 2016) with the requirement that each bin contains at least 30 counts to allow for the use of χ^2 statistics. Figure 2 shows the NICER and NuSTAR light curves for both observations. Figure 3 shows the color–intensity diagrams for these observations. It is evident that the lower flux observation corresponds to the source
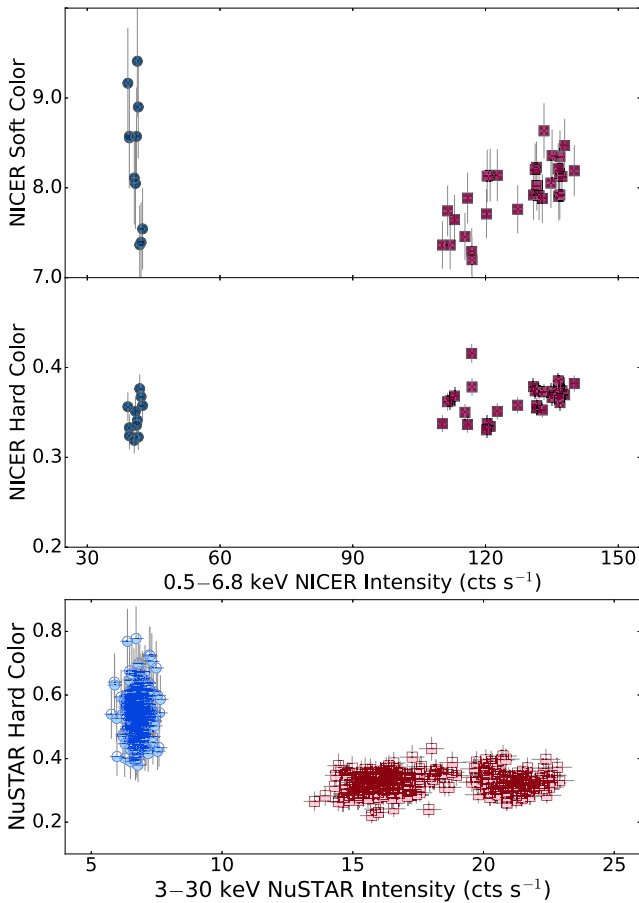
Figure 3. Color–intensity diagrams for NICER and NuSTAR observations of SLX 1735−269. Markers match those used in Figure 2. The top and middle panels represent the soft and hard color in NICER (respectively defined using the bands 1.1–2.0 keV/0.5–1.1 keV and 3.8–6.8 keV/2.0–3.8 keV), and the bottom panel represents the hardest color measurement in NuSTAR, defined using the bands 10–16 keV/6.4–10 keV.

in a hard spectral state, whereas the second observation captured the source in a softer spectral state.

3. Spectral Modeling and Timing Analysis

In this section we discuss the process used to model both the continuum and the reflected emission in the low-flux hard state (Obs 1) and higher-flux soft state (Obs 2), as well as an analysis of some of the timing properties of this system. The NICER spectra are presented in the band from 0.45 to 10 keV, while the NuSTAR spectra are in the 3–40 keV band. Certain regions of both spectra are background dominated. In Obs 1, the very lowest energies ($\lesssim 0.7$ keV) encroach on the background, whereas in Obs 2 the highest energies are background dominated ($\gtrsim 25$ keV), though it is source dominated all the way down to the lowest energies. This is consistent with Obs 1 being in a low hard state ad Obs 2 being in a high soft state.

3.1. Continuum Modeling

We begin by modeling the spectrum of SLX 1735−269 with only a continuum description. This continuum is comprised of a blackbody of temperature, kT_{bb}, representing the thermal emission from the NS, and a cutoff power law representing the illuminating corona with an index of Γ_{pl}. We account for absorption of the continuum along the line of sight with TBABS

Table 2
Continuum

	Obs 1	Obs 2
C_{FPMB}	0.983 ± 0.001	1.001 ± 0.004
C_{NICER}	$0.85^{+0.04}_{-0.08}$	0.89 ± 0.03
$\Delta\Gamma$ (10^{-2})	$-7.0^{+3.6}_{-6.7}$	$-8.6^{+2.4}_{-1.8}$
N_H (10^{22} cm^{-2})	1.62 ± 0.04	1.51 ± 0.02
kT_{bb} (keV)	$0.69^{+0.04}_{-0.06}$	2.01 ± 0.02
$k_{bb}(10^{-3})$	$0.34^{+0.04}_{-0.07}$	3.0 ± 0.1
Γ_{pl}	$1.92^{+0.07}_{-0.02}$	1.7 ± 0.1
$E_{cut,pl}$ (keV)	125^{+123}_{-41}	$5.9^{+0.2}_{-0.3}$
k_{pl}	$0.072^{+0.009}_{-0.003}$	0.25 ± 0.01
χ^2 (dof)	$428(386)$	$676(356)$

Note. All errors are reported at the 90% confidence interval. The blackbody normalization (k_{bb}) is defined as $(L/10^{39}$ erg s$^{-1})/(D/10$ kpc$)^2$, and the power-law normalization (k_{pl}) is defined as photons keV^{-1} cm^{-2} s^{-1} at 1 keV.

with a hydrogen column density of N_H with WILM abundance (Wilms et al. 2000).

We reconcile the calibration differences between NICER and NuSTAR using a model of the form CE$^{-\Delta\Gamma}$ (Steiner et al. 2010). We hold the constant C to be 1 for the NuSTAR focal plane module A (FPMA) spectrum, and fix $\Delta\Gamma = 0$ in both NuSTAR spectra. We allow the constant to vary in the NuSTAR FPMB and in NICER, and allow $\Delta\Gamma$ to vary in NICER to adjust for the difference in slope due to calibration differences.

With the model in place we fit the data for both observations using the XSPEC v12.13.1 (Arnaud 1996). With a reasonable starting place, we then run a Markov Chain Monte Carlo (MCMC) fit in XSPEC with 100 walkers, a burn in of 100,000 and a length of 10,000. The results of that fit are listed in Table 2. We can see that notably the cutoff energy is much lower for Obs 2, indicating alongside Figure 3 that the system entered a softer spectral state. The high-energy cutoff expected for LMXB systems frequently moves to lower energies (Degenaar et al. 2018). This cutoff at lower energies is visible in the shape of the spectra for Obs 2, which can be seen in Figure 4. Obs 1 smoothly follows a single power law within the bounds of these spectra, and so the cutoff energy for this observation should not be considered a physical result. The results of the power-law model in Obs 1 (the harder spectral state) are roughly consistent with David et al. (1997), who find that the continuum can be effectively modeled using an absorbed power law with an index of ~2 (though we may expect the value to vary as the source changes between states). In order to ensure that our results are not affected by the choice of background model, we also fit the continuum using the SCORPEON model,[9] and find that continuum parameters agree within uncertainty for Obs 2, and the fit values agree within uncertainty for all continuum parameters of Obs 1 except for the high-energy cutoff, which again sits outside of the bands of the NuSTAR data, and hence cannot be reliably constrained. Because of this, we opt to continue our analysis using the 3C50 background to minimize the number of free parameters. This is consistent with Partington et al. (2023), which indicates that 3C50 is sufficient even down to source count rates of ~1 count s^{-1}.

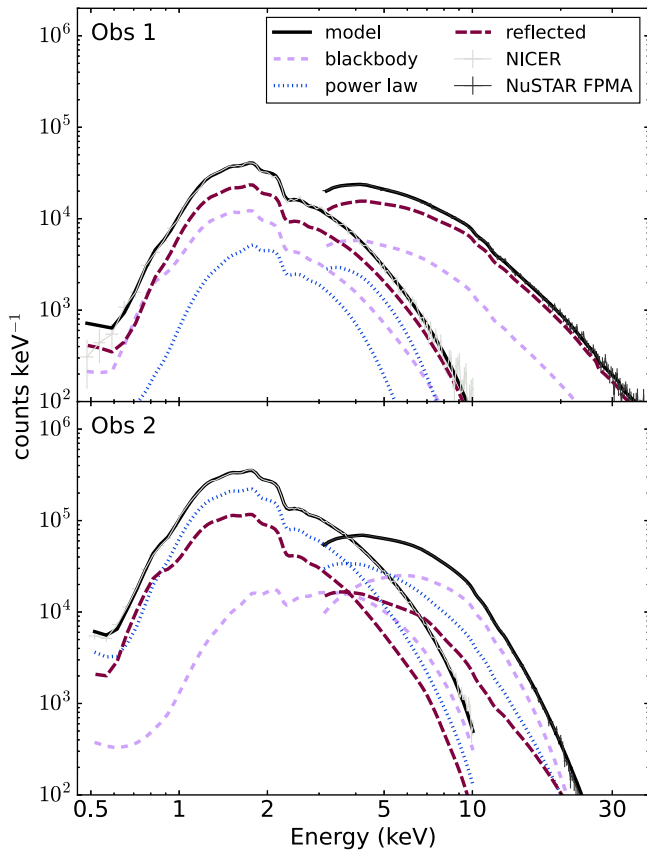[9] https://heasarc.gsfc.nasa.gov/docs/nicer/analysis_threads/scorpeon-overview/

Figure 4. The NICER and NuSTAR spectra in units counts keV^{-1} and the respective model components from XILLVERCO for both observations. We can see here that Obs 1 has an overall lower flux and different shape to that of Obs 2, which displays a cutoff in the power law around 5.8 keV.

Figure 5. Shown here are the regions containing the (top) O VIII Lyα in NICER and (bottom) Fe Kα reflection in NuSTAR FPMA. These are constructed by ignoring the regions surrounding the line in XSPEC, fitting a continuum, then reintroducing these regions and plotting the ratio of the data to the model. The subscripts 15 and 17 refer to the value at which log$N$ is fixed for RELXILLNS in each model. We see strong evidence for a feature around the O VIII energy band, but a feature around the Fe Kα energy band is significantly weaker, at only about 3%–4% above continuum. We show the different models used and find that only XILLVERCO effectively detects the feature in the lower-energy bands.

We look for visual evidence of reflected features by inspecting regions surrounding the expected features. We initially ignore data bins between 0.6 and 0.8 keV (corresponding to the O VIII Lyα feature expected for CO WD UCXBs at around 0.67 keV) and 5.5–7.4 keV (corresponding to the Fe Kα feature around 6.4 keV). We fit the continuum with these regions ignored, then reintroduce them and plot the ratio of the data to the model. The results of this plotting can be seen in Figure 5. We see that the feature around the energy band of Fe Kα peaks at around 4%, quite a bit lower than the 10%–15% seen in some canonical LMXBs (for example, Ser X-1; see Ludlam et al. 2018). However, a very strong feature (around 50% above continuum) is seen at the lowest energies. It should be noted that these features can often be overestimated if other absorption effects such as absorption edges are not accounted for (Ludlam et al. 2021). We find, however, that edges included in the model are poorly constrained and do not significantly impact fit quality, so we exclude these from our model.

To be confident in the existence of these reflection features, we fit our continuum model with two additional Gaussian components. These components have their central energy fixed at 0.67 and 6.4 keV, to account for O VIII and Fe Kα respectively. These Gaussians improve the fit quality in Obs 1 by >5.5σ and Obs 2 by >8.9σ via an F-test, with equivalent widths (EWs) that are often consistent with other reflection features seen in X-ray binaries. For example in Obs 1, the EW is 165 eV for the O VIII feature, which sits on the high end of other measured EWs (see Cackett et al. 2010 for examples of EWs of Fe Kα lines in LMXBs, and Madej & Jonker 2011 for
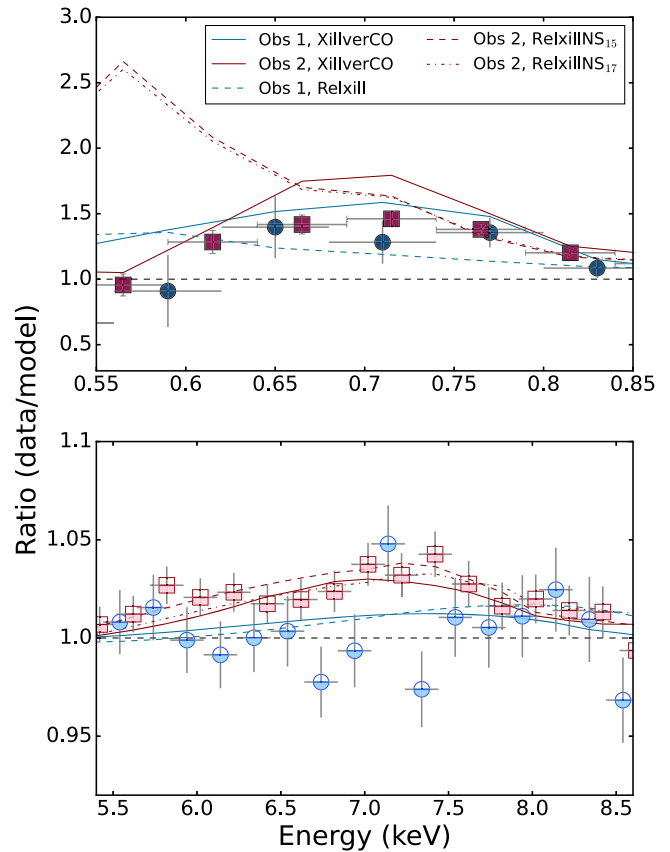
examples of EW in UCXBs). The Fe Kα feature has a high EW value, at around 400 eV. This is reflective of the low contribution of the feature, and indicates that a Gaussian does not effectively pick up any prominent features around 6.4 keV. Similarly, in Obs 2, the EWs for O VIII and Fe Kα are 110 eV and 326 eV, respectively. The values for these Gaussian parameters including their EW and normalization can be found in Table 4 in the Appendix.

To ensure that our detection of emission lines indicative of reprocessed emission does not hinge upon our choice of continuum model, we check their presence with the use of two additional continuum model descriptions utilized for NS LMXBs. These models are an absorbed blackbody with thermal Comptonization (TBABS*(NTHCOMP + BLACKBODY) with NTHCOMP INP_TYPE set to 0 for a blackbody input) and an absorbed disk with thermal Comptonization (TBABS*(NTH-COMP + DISKBB) with NTHCOMP INP_TYPE set to 1 for a disk blackbody input). NTHCOMP is a model which replaces the continuum component often modeled as a simple power law with a more physically motivated thermally Comptonized plasma (Zdziarski et al. 1996; Życki et al. 1999). In each case we find a >5σ improvement to the fit when Gaussian features are included. This is consistent with other similar analyzes, which indicate that the continuum description does not impact

the detection of line features (Coughenour et al. 2018; Ludlam et al. 2020, 2022). The alternative continuum descriptions also display relatively narrow O VIII features, with poorly constrained Fe Kα equivalent widths. The results of these models can also be found in the Appendix. Given the robust detection of the emission lines regardless of continuum model, we proceed with modeling the reprocessed emission with our primary continuum description given the availability of self-consistent reflection models.

3.2. Reflection Modeling

As mentioned previously, the reprocessed emission from an externally illuminated accretion disk contains information about the physical properties of the emitting material in the region close to the compact object, and therefore can be utilized to learn about the properties of the accretor and disk (e.g., chemical composition, ionization state, system inclination, etc.; Ludlam 2024). For testing the chemical composition of the accretion disk, we utilize reflection models that differ significantly in chemical abundance.

First, we apply XILLVERCO, which is a reflection table based on XILLVER (García & Kallman 2010; García et al. 2013) with carbon and oxygen abundances similar to what is seen in CO WDs (i.e., the disk is nearly devoid of H and He while overabundant in C and O). This reflection table has been used in the literature to model the reprocessed emission spectra of several UCXBs (Madej et al. 2014; Ludlam et al. 2021; Moutard et al. 2023). The model produces the reprocessed spectrum assuming primary illumination by a cutoff power law and contains the emergent blackbody component at the emission radius of reflection. We allow the CO abundance (A_{CO}), the disk temperature at the region of reflection (kT_{refl}), the ratio of the incident flux to that of the emergent blackbody flux at the region of reflection ("frac"), and the normalization to be free.[10] We tie the E_{cut} in XILLVERCO to that of the cutoff power law. We fix the redshift to 0 since the source is Galactic.

Because XILLVERCO does not account for the relativistic broadening of reflected features, we must convolve the model with RELCONV, which can be used to determine certain physical parameters of the system (Dauser et al. 2010). Specifically we can use it to determine the inner disk radius at which the reflection is occurring (R_{in}), which we report in terms of the innermost stable circular orbit (R_{ISCO}), the orbit at which a test particle can orbit stably without falling onto the NS, six gravitational radii $R_g = 12.4$ km for a $1.4 M_\odot$, nonrotating NS), assuming the reflection occurs at the innermost region of the disk. In this model we assume that for an NS only one emissivity index is necessary, so we fix both indices to be equal $q_1 = q_2 = q$ and fix the break radius to $500 R_g$ (an obsolete parameter given that there is a single emissivity index). Since the X-rays only probe the innermost region of the disk, we fix the outer disk to $990 R_g$. We tie the inclination measured from RELCONV to that measured with XILLVERCO. We also fix the limb parameter and the dimensionless spin to 0. We choose 0 following Ludlam et al. (2018), who shows that the effect of the spin is minimal for most LMXBs. The fitting process described in Section 3.1 is repeated, and the results are shown in the rightmost two columns of Table 3.

In order to compare the results of a model with UCXB abundances to those with standard solar abundances typical of a standard NS LMXB, we then replace the RELCONV*XILLVERCO in Obs 1 and Obs 2 with RELXILL (García et al. 2014) and RELXILLNS (García et al. 2022), respectively, to account for relativistic reflection. The difference between these models lies in the illuminating source—RELXILLNS assumes the disk is illuminated by a thermal component such as the boundary layer or hot spot on the NS, whereas RELXILL uses a cutoff power law to describe illumination by a hot electron corona. The different spectral states between our two observations necessitates the use of different models accordingly when testing for a disk composed of solar abundance material. Many of the parameters remain the same between all three models, with a few exceptions. For one, in RELXILL and RELXILLNS, the abundance of all elements in the accretion disk are set to solar values with the exception of a variable iron abundance (A_{Fe}).

The reflection fraction f_{refl} parameter in Table 3 represents the ratio of illuminating flux to that which is reflected for RELXILL and RELXILLNS. This is fixed to negative values during fitting in order to only model the reflected component, but the absolute value is reported in Table 3. The ionization state of the material is given by $\log \xi$ (where $\xi = \frac{4\pi}{n} F_x$). RELXILLNS has a variable disk density component ($\log N \, [\text{cm}^{-3}]$) that varies from 15 to 19. We note that both RELXILL and XILLVERCO have fixed disk density of $\log N \, [\text{cm}^{-3}] = 15$ and $\log N \, [\text{cm}^{-3}] = 17$, respectively. To properly compare RELXILLNS to the other models, we perform fits with the density fixed at both 15 (the fixed value in RELXILL; García et al. 2014) and 17 (the fixed value in XILLVERCO; Madej et al. 2014). The results of these models are found in Table 3. Since $\log \xi$ is not a parameter in XILLVERCO, we calculated it using the definition above, where $F_x = \text{frac} \times \sigma T^4$, with the value of temperature T from kT_{refl} in XILLVERCO (see Ludlam et al. 2021 for more information). We use the multiplicative model CFLUX in XSPEC to calculate the unabsorbed fluxes in the 0.5–50 keV band, as well as the absorbed (i.e., measured) flux in the 2–10 keV band. We then use the unabsorbed flux in conjunction with a recent distance measurement from Galloway et al. (2020) to measure the luminosity, $d = 5.8 \pm 0.9$ kpc.[11] We compare this to the empirical Eddington luminosity for a $1.4 M_\odot$ NS $L_{Edd} = 3.8 \times 10^{38}$ erg s^{-1} (Kuulkers et al. 2003) to calculate the Eddington ratio F_{Edd}. Both fluxes and F_{Edd} are reported in Table 3.

Figure 6 shows visually that the non-UCXB models perform worse in the lower energy than XILLVERCO. Because Obs 2 is background dominated above roughly 30 keV, the residuals are dominated by this regime, but we note that RELXILLNS also under performs in this regime. Regardless, XILLVERCO performs about equally well in energy ranges outside of these. We can also see from Figure 5 that the general shape of the low-energy feature is more closely followed by XILLVERCO than either RELXILL or RELXILLNS.

The differences in certain continuum parameters between the models can be explained by continuum model components compensating for a low-energy feature that is not present in the canonical LMXB models. This can be seen in Figure 7, which demonstrates how the power-law and blackbody components

---

[10] See Dauser et al. (2016) and Moutard et al. (2023) for more discussion of the normalization of XILLVERCO and RELXILLNS.

[11] Galloway et al. (2020) poses two possible distances, we opt for the higher of the two to be closer to previously inferred distances of 8.5 kpc (David et al. 1997).

Table 3
Reflection Model Comparison

	Relxill	RelxillNS		XillverCO	
	Obs 1	Obs 1	Obs 2	Obs 1	Obs 2
C_{FPMB}	0.99 ± 0.01	$1.001^{+0.004}_{-0.005}$	1.001 ± 0.003	$0.983^{+0.002}_{-0.005}$	$1.000^{+0.006}_{-0.002}$
C_{NICER}	$0.88^{+0.01}_{-0.02}$	0.83 ± 0.02	0.83 ± 0.01	$0.87^{+0.05}_{-0.03}$	$0.85^{+0.02}_{-0.04}$
$\Delta\Gamma (10^{-2})$	$-3.9^{+0.7}_{-1.0}$	$-12.5^{+1.4}_{-1.7}$	-12.9 ± 0.1	$-5.1^{+4.4}_{-2.5}$	$-11.4^{+1.5}_{-2.9}$
$N_{\mathrm{H}} (10^{22}\ \mathrm{cm}^{-2})$	$1.55^{+0.01}_{-0.04}$	$1.32^{+0.02}_{-0.01}$	1.27 ± 0.01	$1.67^{+0.05}_{-0.03}$	$1.66^{+0.04}_{-0.02}$
kT_{bb} (keV)	$0.67^{+0.04}_{-0.02}$	$1.67^{+0.02}_{-0.04}$	$1.60^{+0.04}_{-0.03}$	0.67 ± 0.03	$2.05^{+0.03}$
$k_{\mathrm{bb}}(10^{-3})$	$0.52^{+0.04}_{-0.03}$	3.4 ± 0.2	3.67 ± 0.05	$0.37^{+0.03}_{-0.05}$	$3.5^{+0.1}_{-0.2}$
Γ_{pl}	1.77 ± 0.01	$0.53^{+0.03}_{-0.05}$	0.149 ± 0.005	$1.93^{+0.04}$	$1.69^{+0.16}_{-0.024}$
$E_{\mathrm{cut,\ pl}}$	$72.7^{+6.2}_{-3.3}$	$1.32^{+0.02}_{-0.05}$	1.05 ± 0.02	145^{+40}_{-36}	$5.0^{+0.6}_{-0.2}$
k_{pl}	$0.036^{+0.003}_{-0.002}$	0.33 ± 0.01	$0.36^{+0.01}_{-0.02}$	0.07 ± 0.01	$0.17^{+0.07}_{-0.01}$
q	$4.8^{+1.1}_{-1.5}$	$10^{\dagger}$	$9.98^{+0.02}_{-0.13}$	$3.6^{+0.9}_{-1.4}$	$2.5^{+2.5}_{-0.5}$
i (deg)	$69.4^{+3.6}_{-3.7}$	$50.1^{+2.8}_{-4.2}$	$46.5^{+2.1}_{-1.3}$	$59.4^{+21.2}_{-3.1}$	$54.9^{+19.0}_{-4.7}$
R_{in} (R_{ISCO})	$1.3^{+0.1}_{-0.2}$	1.8 ± 0.2	$1.51^{+0.03}_{-0.04}$	$1.4^{+2.5}_{-0.4}$	$1.7^{+5.8}_{-0.6}$
A_{CO}	⋯	⋯	⋯	47^{+40}_{-11}	38^{+16}_{-3}
A_{Fe}	$1.9^{+0.2}_{-0.5}$	$0.51^{+0.08}_{-0.01}$	$0.5^{\dagger}$	⋯	⋯
$kT_{\mathrm{xillverCO}}$ $(10^{-2}$ keV)	⋯	⋯	⋯	$8.7^{+0.1}_{-2.1}$	$9.6^{+0.3}_{-0.8}$
$kT_{\mathrm{relxillNS}}$	⋯	2.8 ± 0.1	2.90 ± 0.04	⋯	⋯
frac	⋯	⋯	⋯	$0.11^{+0.11}_{-0.02}$	0.10 ± 0.02
$|f_{\mathrm{refl}}|$	0.9 ± 0.1	$5.1^{+0.3}_{-0.4}$	$5.2^{+0.2}_{-0.1}$	⋯	⋯
$k_{\mathrm{xillverCO}}$ (10^{-9})	⋯	⋯	⋯	$0.5^{+0.5}_{-0.1}$	$3.1^{+1.2}_{-0.4}$
k_{relxill} (10^{-4})	$5.9^{+0.3}_{-0.6}$	0.7 ± 0.1	0.70 ± 0.01	⋯	⋯
$\log N\ (\mathrm{cm}^{-3})$	⋯	15^{a}	17^{a}	⋯	
$\log \xi$	$3.8^{+0.1}_{-0.2}$	3.5 ± 0.1	3.6 ± 0.1	$2.9 \pm 0.5^{\mathrm{b}}$	$3.0 \pm 0.1^{\mathrm{b}}$
F_{2-10} $(10^{-10}\ \mathrm{erg\ s}^{-1}\ \mathrm{cm}^{-2})$	1.93 ± 0.01	5.85 ± 0.01	5.86 ± 0.01	1.93 ± 0.01	5.84 ± 0.01
$F_{0.5-50}$ $(10^{-10}\ \mathrm{erg\ s}^{-1}\ \mathrm{cm}^{-2})$	5.73 ± 0.02	11.26 ± 0.02	11.01 ± 0.02	6.02 ± 0.02	15.98 ± 0.02
F_{Edd} (10^{-2})	0.61 ± 0.01	1.19 ± 0.01	1.17 ± 0.01	0.64 ± 0.01	1.69 ± 0.01
χ^2 (dof)	400 (379)	439 (348)	431(348)	395(378)	415 (349)

Notes.

[a] Parameter is fixed.

[b] Not a model component and is calculated using the description in Section 3.2, using the largest errors for a conservative estimate. All errors are reported at the 90% confidence interval. For comparison some rows are used for both RELXILLNS and XILLVERCO despite having slightly different definitions in their respective models. A_{CO} refers to the carbon and oxygen abundance in XILLVERCO and the iron abundance (A_{Fe}) refers to the Fe abundance in RELXILL and RELXILLNS. frac represents the ratio of the illuminating power law to that of the emergent blackbody from the disk (kT_{refl}) in XILLVERCO, whereas f_{refl} represents the ratio of the illuminating X-rays to those that escape to infinity in both RELXILL and RELXILLNS. The blackbody normalization (k_{bb}) is defined as $(L/10^{39}\ \mathrm{erg\ s}^{-1})/(D/10\ \mathrm{kpc})^2$, and the power-law normalization (k_{pl}) is defined as photons $\mathrm{keV}^{-1}\ \mathrm{cm}^{-2}\ \mathrm{s}^{-1}$ at 1 keV. The normalization for RELXILL and RELXILLNS k_{relxill} scales differently than that of XILLVERCO $k_{\mathrm{xillverCO}}$ so we separate these for ease of reading. $F_{0.5-50}$ refers to the unabsorbed flux in the band 0.5–50 keV, where F_{2-10} refers to the observed flux in the 2–10 keV band. F_{Edd} refers to the Eddington ratio, calculated using the 0.5–50 keV flux and the empirical Eddington luminosity of $3.8 \times 10^{38}\ \mathrm{erg\ s}^{-1}$.

change to adjust to a reflection model that does not encompass the low-energy features. RELXILL and RELXILLNS are both designed with relativistic broadening. Therefore, in order to compare XILLVERCO (which has no broadening inherent to the model) with these models, we must verify that the features detected are also relativistically broadened. We test the spectral broadening by fitting the data both with and without RELCONV, and we find that in Obs 1, the χ^2 improves by 11 for 2 degrees of freedom (dof) with the addition of RELCONV, and in Obs 2 the χ^2 improves by 28 for 2 dof. This implies that the features detected by XILLVERCO are broadened with some degree of significance.

3.3. Timing Analysis

Since the key defining parameter of a UCXB is a period of <80 minutes, we attempt to search for evidence of periodicity in the X-ray light curves. Wijnands & van der Klis (1999) suggests that the inclination angle of the source may be quite high, leading to a smearing of pulsations. A high inclination should result in eclipses in the X-ray light curve, yet none are seen in the data, which is supported by in 't Zand et al. (2007). We search NuSTAR light curves for evidence of periodicity. These light curves were barycenter corrected using the BARYCORR tool in HEASOFT. A search for the presence of periodic signals was performed on the light curves from each of the two individual observations using the Z^2 test (Buccheri et al. 1983). We employed the Z search algorithm in Stingray (Huppenkothen et al. 2019) to perform the search in a grid of frequencies corresponding to periods between 10 and 90 minutes, which is physically motivated based on the expected orbital period range for UCXBs. The search resulted in the detection of peaks (>3σ) only around the harmonics of the NuSTAR orbital period of 96.8 minutes. Based on our analysis we estimate an upper limit on the amplitude of periodic signals in the mentioned frequency range to be 5%–6% with a 99% confidence limit. Further analysis with Fourier methods also yields no significant period measurement. This is, however,
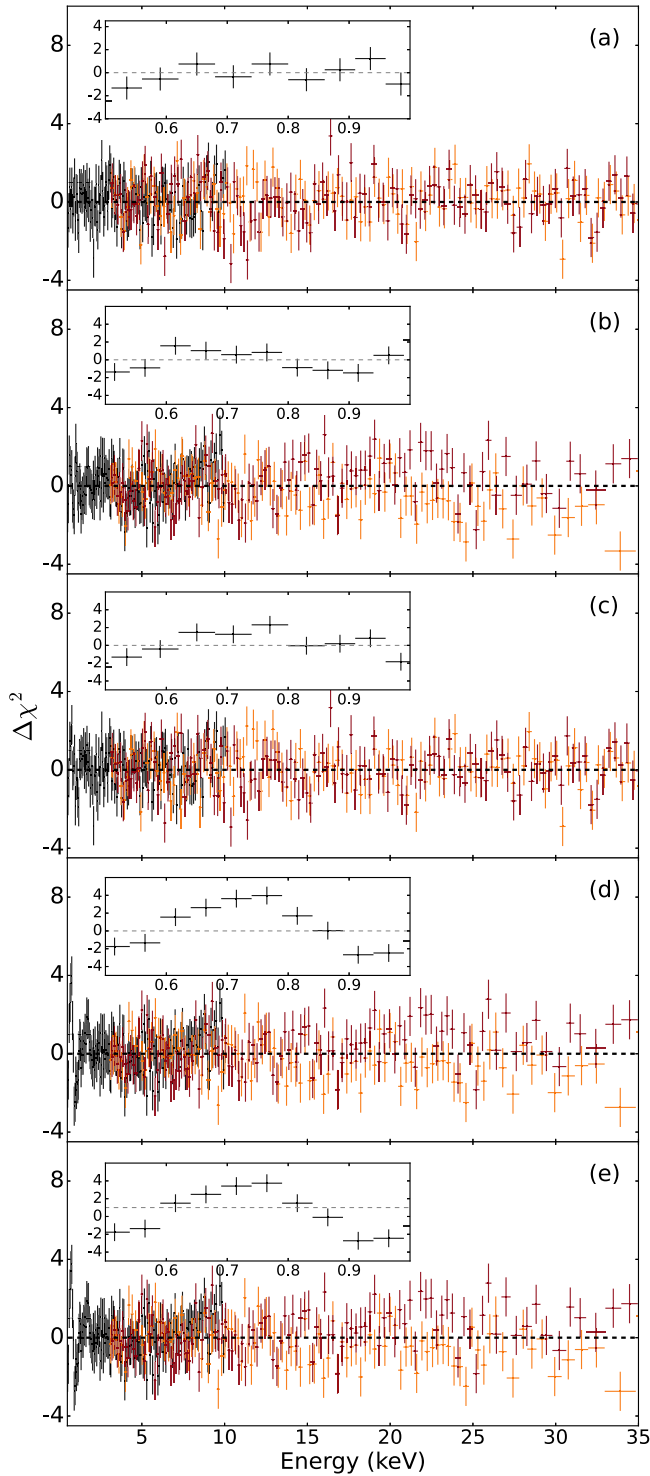
Figure 6. Shown above are the model residuals for the full X-ray band in NICER (black) and NuSTAR (orange/red for FPMA/FPMB respectively). The panels show the residuals for (a) Obs 1 using XILLVERCO, (b) Obs 2 using XILLVERCO, (c) Obs 1 using RELXILL, (d) Obs 2 using RELXILLNS with $\log N = 15$, and (e) Obs 2 using RELXILLNS with $\log N = 17$. The insets display the NICER 0.5–1.0 keV energy range to highlight the difference in fit quality for the area in which we expect an O VIII Lyα for an UCXB.

Figure 7. This plot compares the unfolded spectrum for Obs 2 when modeled with RELXILLNS with logN fixed at 17 to the spectrum modeled with XILLVERCO (the same spectrum shown in Figure 4). We see that the reflection component shifts strongly toward higher energies, and so the power law and blackbody must shift toward lower energies to account for this.

unsurprising, as the short exposures and low count rates of SLX 1735−269 are unlikely to provide strong constraints on any sort of timing analysis. For further discussion of the timing properties see Wijnands & van der Klis (1999), who find that most timing properties of this source are consistent with other NS LMXBs. The exception to this behavior is the power spectrum break frequency, which is anticorrelated with the X-ray flux; this trend is reversed in most NS LMXBs.

4. Discussion and Conclusions

Between the two observations of SLX 1735−269, we find that the spectral shape changes significantly from a power-law-dominated continuum to one dominated by thermal emission with a lower-energy cutoff. We find in Section 3 that the best-fit statistics are achieved using XILLVERCO. Aside from the best-fit statistics, the values retrieved from the fit are also generally more consistent with what we expect from a UCXB. Many of the reported parameters from RELXILLNS in Table 3 are unrealistic. For example in Obs 2, the power-law index is lower than 1, which is lower than the extreme hard spectral state for NSs (Ludlam et al. 2016; Parikh et al. 2017). A_{Fe} in both trials with RELXILLNS is also consistent with the lower bound of the model at 0.5. We also see that in both RELXILL and RELXILLNS, the emissivity index q is unphysically high, approaching the upper bound of 10 for RELXILLNS. We attempt to freeze these values at $q = 3$, a more reasonable value for NSs (Wilkins 2018; Ludlam 2024), but this only serves to worsen the χ^2 further. While this should not be taken as direct support that SLX 1735−269 is in fact a UCXB, this demonstrates that models with higher carbon and oxygen abundances do in fact provide a better explanation for the properties of the X-ray spectrum.
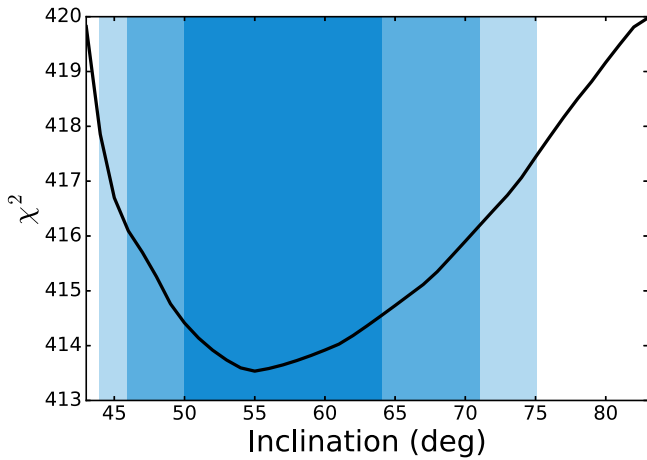
Figure 8. We use the STEPPAR command in XSPEC to determine the sensitivity and quality of fit for the inclination measurement. This steps the best XSPEC fit through values of inclination while allowing all other free parameters to vary. The results may vary from those reported in Table 3, which utilizes the results of MCMC. However, these one-dimensional contours are more conservative limits given the XSPEC STEPPAR routine. We find that an inclination of around 55° is a global minimum, though there is a slightly stronger bias against low inclinations than higher ones. Shown here are the results of STEPPAR for Obs 2. The shaded regions represent the 68%, 90%, and 95% confidence intervals.

It should be noted that the count rates of these spectra are relatively low, especially so for Obs 1, which could affect the quality of the reflection features. Because of this, certain parameters that may be of key interest, such as R_{in}, may not have the most reliable measurements. The R_{in} measurements listed in the XILLVERCO portion of Table 3 indicate that we observe some minor disk truncation during the higher-flux state. We generally expect the disk to move inward at higher luminosities, but magnetic fields can complicate this by truncating accretion disks even at higher luminosities (Cackett et al. 2009; Ludlam et al. 2019). It should be noted, however, that the existence of a feature surrounding the O VIII Lyα energy range and none surrounding Fe Kα prior to any modeling of reflection provides some evidence for nonsolar carbon and oxygen abundances. This is also noted by Koliopanos et al. (2021), who finds that screening by the C and O abundances leads to a diminished Fe Kα feature in the UCXB sources 4U 1543−624 and Swift J1756.9–2508.

We also present in this paper the first tentative measurement of the inclination of SLX 1735−269 at approximately 57^{+23}_{-7} degrees by taking the mean of the XILLVERCO measurements and using the maximum upper and lower bounds of both observations to define the uncertainty. As mentioned above, we do not expect an especially high inclination as we do not observe eclipsing in the light curve. We test whether this parameter is a significant contributor to the statistics in the fit using the STEPPAR command in XSPEC, which varies just one parameter and measures the change in χ^2. We find that there is some degree of sensitivity, with the χ^2 value increasing by approximately 1 at 5° on either side of the measured value, as shown in Figure 8.

After comparing multiple models and attempting various types of analysis, we suggest the following:

1. XILLVERCO appears to provide a better fit for the X-ray spectra of SLX 1735−269 than RELXILL or RELXILLNS, which indicates that the carbon and oxygen abundance deviates from solar. This, alongside the evidence for a lower-energy oxygen feature, suggests that the source is more likely to be a UCXB than a canonical LMXB, strengthening the classification as a UCXB candidate. This is further supported by the fact that only XILLVERCO was able to model the feature in the low-energy band. Relativistic broadening is statistically required to model these features, indicating they are in fact coming from reflection off of the rotating disk.

2. The reflection modeling using XILLVERCO has provided a tentative measurement of the inclination of this system at 57^{+23}_{-7} degrees. The reflection features used to measure both R_{in} and inclination are not very prominent, so further observations with longer exposures are needed to confirm.

3. Our timing analysis is inconclusive. The fact that no eclipses are present in the light curve is consistent with an inclination $\lesssim 80°$. Our Fourier analysis of the system does not reveal any measurable periodicity in the X-ray light curve. This means we cannot conclusively deem the source to be a UCXB by any timing periodicities.

This study provides some additional indirect evidence in support of SLX 1735−269 being a UCXB candidate. We also present an early measurement of the inclination. Future studies using longer exposures in the soft X-rays (for example, from NICER) will be necessary to measure the orbital period and determine whether the source is ultracompact in nature. Optical spectral follow up could potentially provide useful data on the abundance of carbon and oxygen present in the spectrum. Recent missions like XRISM would be useful in resolving reflection features, especially for testing for the existence of the faint Fe Kα in these ultracompact systems (Gandhi et al. 2022).

Appendix
Testing the Presence of Emission Lines by the Addition of Gaussians to Different Continuum Model Descriptions

Table 4 in this Appendix demonstrates the detection of oxygen and iron features in the spectra using a Gaussian component. Regardless of the continuum model used, a gaussian component fixed near the energies of these features significantly improves the fit.

Table 4
Results of Gaussian Fits

	TBABS*(CUTOFFPL+BBODY)		TBABS*(NTHCOMP[0]+BBODY)		TBABS*(NTHCOMP[1]+DISKBB)	
	Obs 1	Obs 2	Obs 1	Obs 2	Obs 1	Obs 2
E_O (keV)	0.67[a]	0.67[a]	0.67[a]	0.67[a]	0.67[a]	0.67[a]
σ_O (10^{-1}) (keV)	8^{+2}_{-1}	12 ± 1	1 ± 0.04	9^{+3}_{-1}	$1.0^{+0.5}_{-0.4}$	0.8 ± 0.2
k_O (10^{-2})	1.3 ± 0.8	$2.3^{+0.8}_{-0.7}$	1.5 ± 0.1	$3.4^{+3.0}_{-2.0}$	$2.4^{+1.4}_{-1.1}$	$2.0^{+0.6}_{-0.7}$
EW_O (eV)	165	110	67	171	59	96
E_{Fe} (keV)	6.4[a]	6.4[a]	6.4[a]	6.4[a]	6.4[a]	6.4[a]
σ_{Fe}	2.0 ± 0.3	1.8 ± 0.2	2.0 ± 0.3	$1.8^{+0.2}_{-0.3}$	2.3 ± 0.4	1.0 ± 0.2
k_{Fe} (10^{-3})	0.7 ± 0.3	$2.0^{+1.6}_{-0.6}$	0.5 ± 0.2	$1.5^{+0.6}_{-0.5}$	0.6 ± 0.3	0.5 ± 0.2
EW_{Fe} (eV)	405	326	262	245	303	75
Significance (σ)	>5.6	>8.9	>5.1	>8.9	>5.0	>5.2

Note.
[a] Indicates fixed value, same for all fits. Parameters with a subscript O refer to those measured around the expected O VIII feature and those with the subscript Fe refer to the Fe Kα feature. The normalization k is in units photons cm^{-2} s^{-1}. EW is the equivalent width of the feature, measured using the EQWIDTH command in XSPEC. Significance refers to the improvement over the respective continuum model via an F-test.

ORCID iDs

D. L. Moutard ⬤ https://orcid.org/0000-0003-1463-8702
R. M. Ludlam ⬤ https://orcid.org/0000-0002-8961-939X
M. Sudha ⬤ https://orcid.org/0000-0003-0440-7978
E. M. Cackett ⬤ https://orcid.org/0000-0002-8294-9281
N. Degenaar ⬤ https://orcid.org/0000-0002-0092-3548
A. C. Fabian ⬤ https://orcid.org/0000-0002-9378-4072
P. Gandhi ⬤ https://orcid.org/0000-0003-3105-2615
J. A. García ⬤ https://orcid.org/0000-0003-3828-2448
A. W. Shaw ⬤ https://orcid.org/0000-0002-8808-520X
J. A. Tomsick ⬤ https://orcid.org/0000-0001-5506-9855

References

Arnaud, K. A. 1996, in ASP Conf. Ser. 101, Astronomical Data Analysis Software and Systems V, ed. G. H. Jacoby & J. Barnes (San Francisco, CA: ASP), 17
Bahramian, A., & Degenaar, N. 2023, in Handbook of X-ray and Gamma-ray Astrophysics, ed. C. Bambi & A. Santangelo (Singapore: Springer), 120
Bazzano, A., Cocchi, M., Ubertini, P., et al. 1997, IAU Circ., 6668
Buccheri, R., Bennett, K., Bignami, G. F., et al. 1983, A&A, 128, 245
Cackett, E. M., Altamirano, D., Patruno, A., et al. 2009, ApJL, 694, L21
Cackett, E. M., Miller, J. M., Ballantyne, D. R., et al. 2010, ApJ, 720, 205
Cackett, E. M., Miller, J. M., Bhattacharyya, S., et al. 2008, ApJ, 674, 415
Coughenour, B. M., Cackett, E. M., Miller, J. M., et al. 2018, ApJ, 867, 64
Chen, W.-C., Liu, D.-D., & Wang, B. 2020, ApJL, 900, L8
Cumming, A., Macbeth, J., in 't Zand, J. J. M., et al. 2006, ApJ, 646, 429
Dauser, T., García, J., Walton, D. J., et al. 2016, A&A, 590, A76
Dauser, T., Wilms, J., Reynolds, C. S., et al. 2010, MNRAS, 409, 1534
David, P., Goldwurm, A., Murakami, T., et al. 1997, A&A, 322, 229
Degenaar, N., Ballantyne, D. R., Belloni, T., et al. 2018, SSRv, 214, 15
Fabian, A. C., Rees, M. J., Stella, L., et al. 1989, MNRAS, 238, 729
Galloway, D. K., in't Zand, J., Chenevez, J., et al. 2020, ApJS, 249, 32
García, J., Dauser, T., Lohfink, A., et al. 2014, ApJ, 782, 76
García, J. A., Dauser, T., Ludlam, R., et al. 2022, ApJ, 926, 13
García, J., Dauser, T., Reynolds, C. S., et al. 2013, ApJ, 768, 146
García, J., & Kallman, T. R. 2010, ApJ, 718, 695
Gandhi, P., Kawamuro, T., Díaz Trigo, M., et al. 2022, NatAs, 6, 1364
Huppenkothen, D., Bachetti, M., Stevens, A. L., et al. 2019, ApJ, 881, 39
in't Zand, J. J. M., Jonker, P. G., & Markwardt, C. B. 2007, A&A, 465, 953
Kaastra, J. S., & Bleeker, J. A. M. 2016, A&A, 587, A151
Koliopanos, F., Gilfanov, M., Bildsten, L., et al. 2014, The X-ray Universe, 2014, 102
Koliopanos, F., Vasilopoulos, G., Guillot, S., et al. 2021, MNRAS, 500, 5603
Kuulkers, E., den Hartog, P. R., in't Zand, J. J. M., et al. 2003, A&A, 399, 663
Ludlam, R. M. 2024, Ap&SS, 369, 16
Ludlam, R. M., Cackett, E. M., García, J. A., et al. 2020, ApJ, 895, 45
Ludlam, R. M., Cackett, E. M., García, J. A., et al. 2022, ApJ, 927, 112
Ludlam, R. M., Jaodand, A. D., García, J. A., et al. 2021, ApJ, 911, 123
Ludlam, R. M., Miller, J. M., Arzoumanian, Z., et al. 2018, ApJL, 858, L5
Ludlam, R. M., Miller, J. M., Barret, D., et al. 2019, ApJ, 873, 99
Ludlam, R. M., Miller, J. M., Bachetti, M., et al. 2017, ApJ, 836, 140
Ludlam, R. M., Miller, J. M., Cackett, E. M., et al. 2016, ApJ, 824, 37
Madej, O. K., García, J., Jonker, P. G., et al. 2014, MNRAS, 442, 1157
Madej, O. K., & Jonker, P. G. 2011, MNRAS, 412, L11
Matsuoka, M., Kawasaki, K., Ueno, S., et al. 2009, PASJ, 61, 999
Molkov, S., Revnivtsev, M., Lutovinov, A., et al. 2005, A&A, 434, 1069
Moutard, D. L., Ludlam, R. M., García, J. A., et al. 2023, ApJ, 957, 27
Miller, J. M., Parker, M. L., Fuerst, F., et al. 2013, ApJL, 779, L2
Nelson, L. A., Rappaport, S. A., & Joss, P. C. 1986, ApJ, 304, 231
Parikh, A. S., Wijnands, R., Degenaar, N., et al. 2017, MNRAS, 466, 4074
Partington, E. R., Cackett, E. M., Kara, E., et al. 2023, ApJ, 947, 2
Remillard, R. A., Loewenstein, M., Steiner, J. F., et al. 2022, AJ, 163, 130
Savonije, G. J., de Kool, M., & van den Heuvel, E. P. J. 1986, A&A, 155, 51
Skinner, G. K., Willmore, A. P., Eyles, C. J., et al. 1987, Natur, 330, 544
Steiner, J. F., McClintock, J. E., Remillard, R. A., et al. 2010, ApJL, 718, L117
Syunyaev, R. A., Arefev, V. A., Borozdin, K. N., et al. 1991, SvAL, 17, 409
Wijnands, R., & van der Klis, M. 1999, A&A, 345, L35
Wilkins, D. R. 2018, MNRAS, 475, 748
Wilms, J., Allen, A., & McCray, R. 2000, ApJ, 542, 914
Wilson, C. A., Patel, S. K., Kouveliotou, C., et al. 2003, ApJ, 596, 1220
Zdziarski, A. A., Johnson, W. N., & Magdziarz, P. 1996, MNRAS, 283, 193
Zolotukhin, I. Y., & Revnivtsev, M. G. 2011, MNRAS, 411, 620
Życki, P. T., Done, C., & Smith, D. A. 1999, MNRAS, 309, 561